Research article

Valorization of the treatment of antibiotic and organic contents generated from an in-situ-RAS-like shrimp farming pond by using graphene-quantum-dots deposited graphitic carbon nitride photocatalysts

Nguyen Thi Phuong Thao [a], Nguyen Le Minh Tri [a], Tran Trung Kien [a], Tra Van Tung [a], Tran Thi Hieu [a], Nguyen Viet Thang [a], Le Thanh Son [a], Tran Le Luu [b], Hans Schnitzer [c], Hai Le Thanh [a],[*]

[a] Institute for Environment and Resources, National University of Ho Chi Minh City, Ho Chi Minh 740500, Viet Nam
[b] Master Program in Water Technology, Reuse and Management, Vietnamese – German University, Binh Duong, Viet Nam
[c] Institute for Process and Particle Engineering, Graz University of Technology, Graz A-8010, Austria

A R T I C L E I N F O

A B S T R A C T

In this study, we investigated the possibility of a photocatalytic system that uses graphene-quantum-dot (GQD)-deposited graphitic carbon nitride (g-C3N4) to treat tetracycline (TC) and other organic compounds generated from an in-situ-recirculatory-aquaculture-system (RAS)-like shrimp farming pond. GQDs were successfully deposited on the exfoliated g-C3N4 base through a hydrothermal treatment. The results showed that the incorporation of GQDs into the g-C3N4 enhanced its porosity without aggregating its mesoporous structure. The GQDs-deposited g-C3N4 photocatalysts revealed sheet-like structures with nanopores on their surface that facilitate photocatalysis. More than 90% of the TC was removed by the photocatalysts under UV-LED irradiation. Low loadings of GQDs over g-C3N4 resulted in a faster and more effective photocatalysis of TC, mainly driven by.O2- radicals. The photocatalysts were also applicable in the degradation of organic compounds with 27% of the total organic compounds (TOC) being removed from the wastewater of a RAS-like shrimp farming pond.

1. Introduction

Carbon quantum dots (CQDs), a new class of fluorescent carbon nanomaterial, have gained attention due to having features such as unique optical properties, high catalytic activity, and good biocompatibility at a low cost. With these properties, CQDs have been assembled with various porous materials such as zeolites, carbonaceous porous materials, mesoporous silica, porous metallic compounds, metal-organic frameworks (MOFs), and porous g-C$_3$N$_4$ for use in a wide range of applications such as biomedicine, sensing, electrochemistry, optics and photocatalysis [1]. When CQDs are incorporated with porous media, it not only compensates for the shortcomings of the CQDs in these applications but also produces new functionalities through synergetic interactions to extend to new applications [1,2].

---

* Corresponding author.
  E-mail address: haile3367@yahoo.com (H. Le Thanh).

Compared to CQDs that are quasi-spherical carbon nanoparticles at sizes below 10 nm, graphene quantum dots (GQDs) are small fragments of single- or few-layers of graphene with sizes of a few nm up to 100 nm [3]. GQDs also exhibit extraordinary opto-electronic properties. The application of GQDs has been reported in many studies [4–6]. Despite extensive research, reports on the facile coupling of g-C_3N_4 with GQDs are not discernible for the application in treatment of discharged wastewater from a shrimp pond [7].

With tremendous achievements obtained since the third industrial revolution, society has been facing increasing concerns related to the energy crisis and environmental pollution due to the large consumption of fossil fuels (natural gas, coal and petroleum), which are being depleted rapidly [8]. Therefore, it is essential to seek out advanced technologies to minimize environmental pollution and solve the energy crisis. Recently, scientists have come up with an artificial route that utilizes solar energy [9], developing photo-catalytic semiconductors capable of harvesting solar light with the ability to degrade environmental pollutants. Since the pioneering work on water photolysis using the TiO_2 photocatalyst, research in this field using UV-responsive and visible-light-responsive photocatalysts, including titania-based and non titania based materials (ZnO, Fe_2O_3, CdS, Bi_2WO_6, $BiVO_4$, Ta_2O_5, Ta_3N_5, TaON, etc.), has been carried out [10–15]. Due to the intrinsically large band gap energy of semiconductors, it is essential to discover robust semiconductors with narrow band gap energy, leading to a growing interest in the development of a polymeric semiconductor, namely graphitic carbon nitride (g-C_3N_4). This has a low cost, high physicochemical stability and unique electronic band structure [16–21]. However, its high recombination of photo-generated electrons and holes, low surface area and insufficient light absorption has led to unfavorable photocatalytic activity in g-C_3N_4 [22]. Consequently, it is important to develop strategies to improve the photocatalytic performance of g-C_3N_4 [23].

In order to overcome the shortcomings of g-C_3N_4, coupling g-C_3N_4 with other semiconductors has been applied recently. For example, Wang et al. (2019) reported the enhanced separation and migration of photo-induced charges after the introduction of a Z-scheme configuration of g-C_3N_4 and TiO_2 microflowers [24]. Another study led by He et al. (2018) demonstrated the remarkable combination of photo-degradation and the air-oxidation of phenol over direct Z-scheme Bi_2O_3/g-C_3N_4 photocatalysts [25]. Razavi-Esfali et al. (2022) constructed a novel ultrathin g–C_3N_4 coupled with WO_3, which had a superior photocatalytic performance towards the alleviation of organic compounds [26]. In addition to constructing heterojunctions in g-C_3N_4, elemental doping is another approach to improving its photocatalytic activity [27,28]. For instance, Bui et al. (2020) fabricated Ba-doped g-C_3N_4 with a remarkable photocatalytic efficiency for tetracycline (91.94 %) [29]. Chen et al. (2021) successfully synthesized Co-doped g-C_3N_4 nanosheets to act as photocatalysts involving a highly photocatalytic production of H_2 (808.92 mmol g^{-1} h^{-1}) and the degradation of MB (96 %) [30]. Although positive results have been obtained by these two approaches, chemical modifications of g-C_3N_4 are costly and not benign to the environment. Hence, searching for another cheaper and greener modifier is of interest.

Shrimp farming is an important sector of the aquaculture industry that contributed 114.5 million tons of product to the global aquaculture product total in 2018 [31]. According to FAO, 64% of shrimp production comes from shrimp farming [31]. There are two shrimp species dominant in shrimp farming, the white leg shrimp (Litopenaeus vannamei) and the black tiger shrimp (Penaeus monodon). They have been popularly traded in Asia and America, particularly in top-of-the-world aquaculture producers like Bangladesh, China, India, Vietnam, and Indonesia, where the replacement of extensive shrimp farming by intensive farming with high productivity has occurred [32,33]. However, the occurrence of epidemics and pandemics caused by viruses, bacteria, and other pathogens has significantly affected global shrimp productivity in recent years [34]. As a part of global shrimp production, the productivity of shrimp farming in Vietnam has also been greatly affected by diseases. It has been noted that shrimp farming has been a major source of income for many Vietnamese households over the decades. Therefore, the livelihoods of these households are insecure due in part to these unexpected events. To prevent the aggressiveness of the diseases causing mortalities to shrimp, the application of a variety of antibiotics to shrimp farming is inevitable, although recirculatory aquaculture systems (RAS) have been known to be an effective system to manage the biosecurity of shrimp farming [35–37]. This has caused the discharge of wastewater from shrimp farms to be contaminated by residual pharmaceuticals. Other than that, a high content of other organic compounds generated during shrimp breeding was also found in the discharged wastewater from shrimp ponds. These compounds resulted in high risks to the surrounding ecosystem and human health [38]. **Therefore, it is necessary to minimize the presence of these compounds in the discharged aqueous solutions of shrimp ponds, which is a challenging task.**

Although various physical and biological adsorption technologies are applicable for use in the treatment of such pollutants, they are not appropriate for the degradation of antibiotics and other specific organic compounds [29,39]. Photocatalysis driven by photocatalysts has drawn considerable attention for use in the amelioration of antibiotics due to its potential to degrade antibiotics into small molecules like CO_2 and H_2O [40–43]. To the best of our knowledge, a comprehensive investigation of the photocatalytic activities of GQDs-deposited g-C_3N_4 photocatalysts for the degradation of TC and their possible application in the degradation of organic pollutants discharged from the wastewater of shrimp ponds has not yet been conducted. Inspired by the aforementioned studies, in this study, we developed metal-free g-C_3N_4 photocatalysts modified with GQDs through thermal polymerization and hydrothermal treatments so as to overcome the drawbacks of g-C_3N_4 for the enhancement of its photocatalytic activity. The experimental parameters that affected the efficiency of TC alleviation over the prepared photocatalysts through adsorption, photolysis, and photocatalysis will also be studied. The kinetics and mechanisms of the processes were also discussed in detail. Moreover, we aimed to apply the g-C_3N_4 photocatalysts with an improved photocatalytic performance to the photocatalytic degradation of tetracycline (TC), a broad-spectrum antibiotic commonly used in shrimp farms in Vietnam (21%), and the organic content of discharged wastewater from a local RAS-like shrimp pond [29,44,45].

2. Experimental section

2.1. Preparation of GQDs

Typically, 1 g of glucose (Sigma-Aldrich, USA) was dissolved in 100 mL of distilled (DI) water under mild ultrasonication (JAC 4020 model) for 15 min. The mixture was then transferred to a Teflon-lined autoclave and heated in an oven for 4 h. After cooling to room temperature, the resultant dark-brown solutions were then used for dialysis through a dialysis tube (MWCO ~ 10,000 Da, Millipore). Afterwards, the yellow GQD solutions were dried at 60 °C in a vacuum oven to obtain solids.

2.2. Preparation of the g-C$_3$N$_4$ and the GQDs-deposited g-C$_3$N$_4$ photocatalysts

Typically, dicyanamide (Sigma-Aldrich) was put into a crucible with a cover and then placed in a muffle furnace for calcination at 550 °C with a heating increment of 1 °C/min in 4h. g-C$_3$N$_4$ was obtained after the thermal polymerization, and then ground into powder by using a mortar. For the synthesis of the GQDs – C$_3$N$_4$ composites, dicyanamide was separately mixed with certain aliquots (5 and 10 mL) of the GQDs solution. The mixtures were then transferred to a crucible with a cover for further calcination at 550 °C with a heating rate of 1 °C/min in 4h. The obtained powder was washed with DI water, collected by centrifugation, and finally dried in the oven at 60 °C to get the GQDs-deposited g-C$_3$N$_4$ photocatalysts denoted as 5CD@g-C$_3$N$_4$ and 10CD@g-C$_3$N$_4$. The synthesis method is illustrated in Scheme 1.

2.3. Characterization

The crystal structure was characterized by X-ray diffraction (XRD) using an X-ray diffractometer with Cu Kα radiation (λ = 0.154056 nm). Transmission electron microscope (TEM) and high-resolution TEM (HRTEM) images were obtained with a JEOL JEM-2100F (200 kV). The functional groups of g-C$_3$N$_4$ and CD@g-C$_3$N$_4$ composites were studied using Fourier Transform IR (FTIR) spectroscopy. Diffuse reflectance spectra (DRS) of samples were recorded in the wavelength range of 200–800 nm. The diffuse reflectance spectra were converted into absorbance and Kubelka-Munk (K-M) forms. The specific Brunauer–Emmett–Teller (BET) surface area and pore size measurements of samples were conducted on a Quantachrome apparatus at 77.3 K under nitrogen gas. Before the BET measurement, the samples were degassed in a flow of N$_2$ at 300 °C for 5 h. The specific surface area was determined by the Brunauer–Emmett–Teller method. The pore size distribution was calculated using Barrett-Joyner-Halenda (BJH) desorption branches of the isotherms. Photocurrent response of composites was recorded on a potentiostat (VSP, Biologics) using a conventional three-electrode cell with a coiled Pt wire and an Ag/AgCl (saturated KCl solution) electrode as the counter and reference electrodes, respectively. The working electrode was fabricated by the dispersion of 5 mg of samples in 1 mL of ethylene glycol solution to make a slurry, followed by spreading it on a 2 cm × 2 cm ITO glass substrate with an active area of about 2 cm × 1 cm, and then drying the working electrode at 60 °C. The three electrodes were immersed in a 0.5 M Na$_2$SO$_4$ solution (pH 6.4). The working electrode was exposed to a UV-LED (365 nm, 500 W) light source in each light on-off cycle (30 s/cycle) at an applied potential of 0 V (vs. NHE).

2.4. The photo-degradation of TC over the photocatalysts

The photocatalytic activity of the synthesized materials was evaluated through the photo-degradation of a prototype antibiotic TC under UV-LED (365 nm, 500 W) irradiation. In a typical experiment, 80 mg of the photocatalyst was added to 50 mL solution of TC with a certain concentration stored in a 250 mL glass beaker. Before light irradiation, the suspension was mixed in the dark under vigorous stirring for 60 min to acquire the adsorption-desorption equilibrium. The photocatalytic system was subsequently illuminated and

Scheme 1. Schematic diagram of the synthesis methods of GQDs (a) and CD@g-C$_3$N$_4$ (b).

stirred for 120 min to observe the time-dependent degradation of TC. The pH of the solution was adjusted by adding 0.1 M NaOH or HCl to the aqueous solution.

During the photocatalytic process, an aliquot (3.0 mL) of TC solution was taken out of the photocatalytic system after an interval of 15–30 min into the process. The obtained solution was passed through another centrifugation process (3000 rpm) for 3 min. The concentration of the left-over TC after the degradation was determined with the aid of a UV–Vis spectrometer. The degradation efficiency (CDE, %) of TC was determined as follows in Equation (1):

$$CDE \, (\%) = (C_o - C_t) \, *100/ \, C_o \tag{Eq. 1}$$

where C_o is the initial concentration of TC (mg/L) and C_t is the concentration of TC at the time t (min).

3. Results and discussion

3.1. Morphological and structural characterization

The morphology of g-C$_3$N$_4$ synthesized via the thermal condensation revealed the stacking structure of the thin, porous layers of the bulk g-C$_3$N$_4$ with carbon (C) and nitrogen (N) as the major chemical compositions as seen in the TEM images in Fig. 1(a–c). Meanwhile, the TEM image of GQDs (Fig. 1d) shows the presence of dots with sizes of a few nanometers.

The deposition of GQDs on g-C$_3$N$_4$ is revealed in Fig. 2a and b, where 5CD@g-C$_3$N$_4$ revealed a sheet-like structure with nanopores on the surface that would facilitate photocatalysis [46,47], while GQDs displayed an interplanar spacing of 0.32 nm, consistent with the previous study [4], and exhibited a hexagonal crystalline structure through the 2D fast Fourier transform (FFT) pattern (Fig. 2c). The selected area electron diffraction (SAED) pattern of GQDs deposited on g-C$_3$N$_4$ revealed the crystal planes (101), (200), and (220) corresponding to the d-spacing of 0.31 nm, 0.20 nm, and 0.16 nm of GQDs (Fig. 2d). Their XRD pattern (Fig. 2e) also shows a broad peak at 2θ = 0.24°, corresponding to the d-spacing of 0.37 nm in the (200) plane [5]. This d-spacing value is broader than that of graphite due to the presence of oxygen-containing functional groups in GQDs [6].

Meanwhile, g-C$_3$N$_4$ typically shows an intense (002) peak of stacking interlayered heptazine (C$_6$H$_7$) units at 2θ = 27.4° and a weaker (100) peak of in-planar nitrogen pores at a lower angle (Fig. 3). The intensity of the (002) peak of g-C$_3$N$_4$ was remarkably decreased after the deposition of GQDs, indicating a decrease in the size of stacking layers along the c-axis as they moved from the bulk to the nanostructure domain [48]. This phenomenon was evidenced by the distortion of the (100) peak [26,48]. With respect to the pristine g-C$_3$N$_4$, the enlarged XRD shows that the peak derived from the periodic stacking of nanosheets was slightly shifted to a lower angle, and the same phenomenon was also observed for the other peak. The intensity of the two peaks became weaker. These are the indicators of the increased distance between the g-C$_3$N$_4$ layers and also between the nitrogen pores due to the exfoliation of the bulk g-C$_3$N$_4$ and successful introduction of GQDs into the g-C$_3$N$_4$ matrix [30].

In addition to XRD, FTIR was employed to study the functional groups of g-C$_3$N$_4$ and 5CD@g-C$_3$N$_4$ (Fig. 4a). The characteristic peaks of the s-triazine rings and C–N and C═CN heterocycles in the g-C$_3$N$_4$ structure can be clearly identified at 810 cm^{-1} and in the region of 1200–1700 cm^{-1} [48,49]. Moreover, a broaden peak located at 3000–3500 cm^{-1} corresponds to the vibration modes of the N–H groups and O–H adsorbed water molecules due to the incomplete polymerization of the precursor [49]. Meanwhile, the FTIR spectrum of GQDs represents the vibrations of O–H, C–H, C═C and C═O, which were derived from the conjugated carbon structure of GQDs and their functional groups such as hydroxyl, carboxylic acid and epoxy [50]. However, the FTIR signals of GQDs were not clearly found in the FTIR spectrum of 5CD@g-C$_3$N$_4$, mainly due to the strong vibration of C–N of g-C$_3$N$_4$ and the low loading amount of GQDs [49,51]. Meanwhile, all of the peaks of g-C$_3$N$_4$ were retained in the FTIR spectrum of 5CD@g-C$_3$N$_4$, suggesting the sustainability of the g-C$_3$N$_4$ framework after the loading of GQDs. Therefore, these surface functional groups of 5CD@g-C$_3$N$_4$ are vital for its enhanced photocatalytic activity.

The surface area and porosity of the photocatalysts are two of the key factors affecting their photocatalytic activity. These parameters were obtained through BET analysis with the data shown in Table 1.

The adsorption-desorption isotherms of g-C$_3$N$_4$ and 5CD@g-C$_3$N$_4$ (Fig. 4b) obtained by the accumulation of N$_2$ gas on the surface of the catalysts revealed type IV isotherms with the H3-type hysteresis in the P/P$_0$ range of 0.4–1.0, which are characteristic of mesoporous structures with cylindrical pores according to the classification of the International Union of Pure and Applied Chemistry (IUPAC) [52,53]. Their adsorption edges are observed at values of P/P$_0$ = 0.8–10, indicating the presence of macropores in addition to
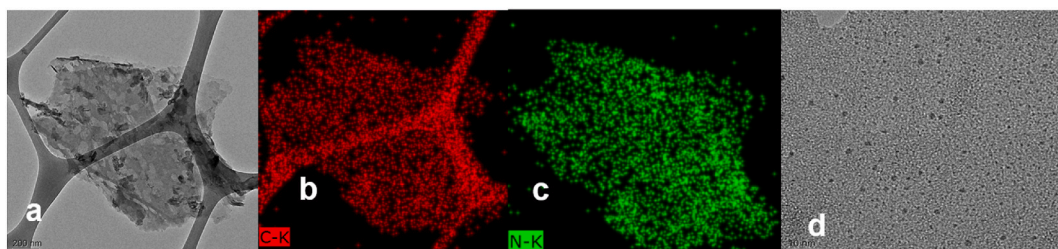

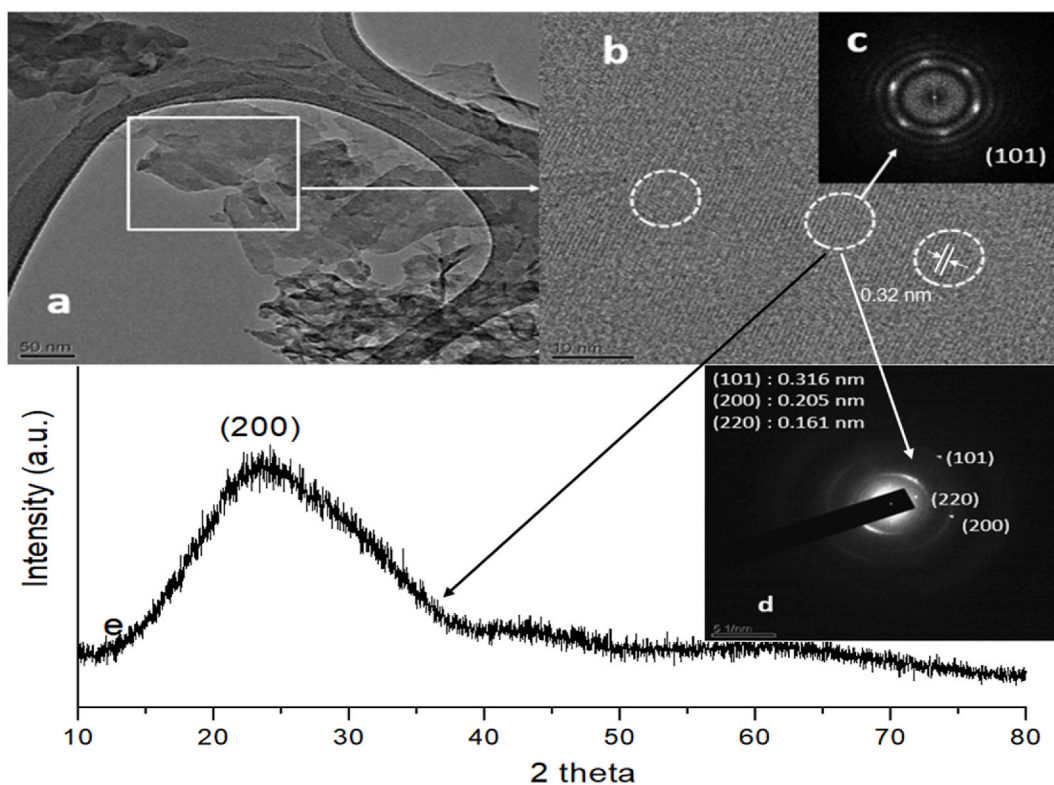**Fig. 1.** TEM images of g-C$_3$N$_4$ (a–c) and GQDs (d).

Fig. 2. TEM and HR-TEM images of 5CD@g-C$_3$N$_4$ (a,b). SAED, FFT, and XRD patterns of GQDs (c, d, e).
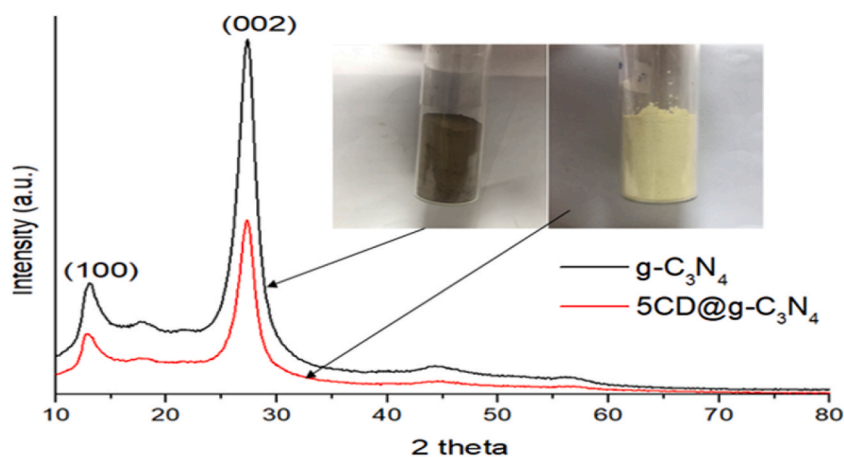

Fig. 3. XRD patterns of g-C$_3$N$_4$ and 5CD@g-C$_3$N$_4$. (The inset: the images of g-C$_3$N$_4$ and 5CD@g-C$_3$N$_4$).

mesopores [26,52]. Also, the "two step" characteristics of the desorption branches of the isotherms of g-C$_3$N$_4$ and 5CD@g-C$_3$N$_4$ suggested the two maximum values of their pore size distribution [54], consistent with the pore size distribution shown in Fig. 4c. It is noted that the average pore sizes of the two materials are in the range of 2–50 nm, confirming their meso-porous structures. Compared with g-C$_3$N$_4$, 5CD@g-C$_3$N$_4$ exhibited a much higher surface area and pore volume due to the exfoliation of the bulk g-C$_3$N$_4$ during the production of 5CD@g-C$_3$N$_4$. These results are not consistent with the study of Deng et al. (2017) [51]. In their study, they reported a decrease in the surface area of g-C$_3$N$_4$ nanosheets after the loading of N-GQDs. However, our study is in agreement with that of Y. Jiao et al. (2019) [55]. Obviously, the incorporation of GQDs into the bulk g-C$_3$N$_4$ enhanced the porosity of g-C$_3$N$_4$ without aggregating its meso-porous structure, which is different from the previous study [56]. Interestingly, its enhanced surface area and enlarged pore volume can provide more active sites for its absorption of target contaminant molecules, facilitating the mass transfer between it and the target molecules, and improving its light harvesting ability, contributing to the highly photocatalytic performance of the
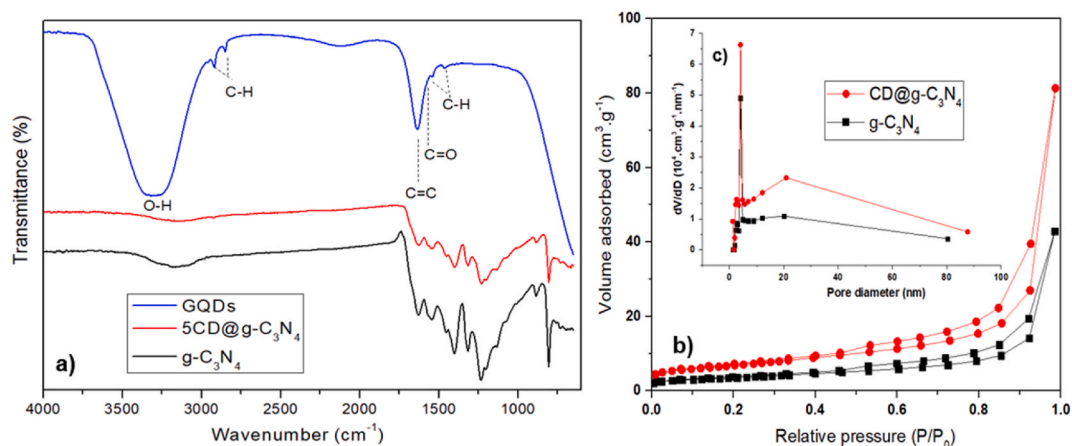
Fig. 4. (a) FTIR spectra of GQDs, g-C$_3$N$_4$, and 5CD@g-C$_3$N$_4$. (b) Adsorption-desorption isotherms of g-C$_3$N$_4$ and 5CD@g-C$_3$N$_4$. (c) Pore size distribution of g-C$_3$N$_4$ and 5CD@g-C$_3$N$_4$.

Table 1
BET parameters and band-gap values of the photocatalysts.

Sample	Surface area (m^2.g^{-1})	Pore volume (cm^3.g^{-1})	Pore diameter (nm)	Band gap (eV)
g-C$_3$N$_4$	14.22	0.066	4.0	2.81
5CD@g-C$_3$N$_4$	26.95	0.12	4.0	2.69

photocatalyst [51].

3.2. Light absorption properties

To elucidate the light absorption ability of g-C$_3$N$_4$ after the introduction of GQDs, it was necessary to gain more insights into their optical properties through the UV–Vis absorption spectra. It is noted that the synthesized GQDs exhibited strong UV light absorption with an extension to visible light (Fig. 5a). The absorption portion below 300 nm was due to the π- π* transition of C=C sp2 carbons in the aromatic rings of GQDs, while the absorption portion above 300 nm was ascribed to the n- π* transition of the C=O carbon core and the C=O surface state transition with a lone pair of GQDs, respectively [50,57]. When it comes to g-C$_3$N$_4$, it shows that g-C$_3$N$_4$ has the ability to absorb not only in the UV region but also in visible light (Fig. 5b). Its absorption edge lies at 550 nm. After the deposition of GQDs, 5CD@g-C$_3$N$_4$ exhibited a remarkably enhanced absorbance in the UV light and visible light regions where the UV absorbance was higher than the visible light one. It is noted that the absorption edge of 5CD@g-C$_3$N$_4$ was red-shifted, which was attributed to the
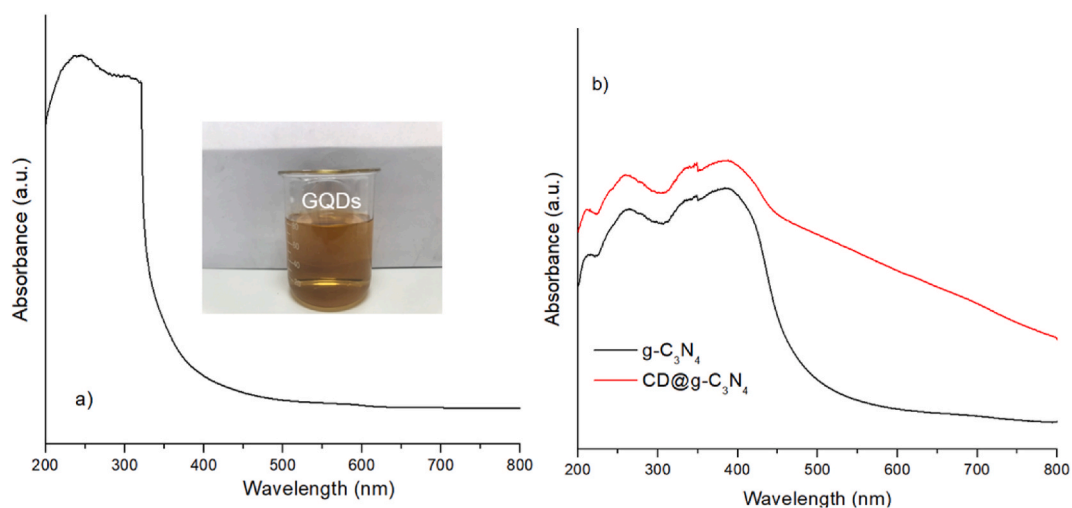

Fig. 5. The UV-VIS spectra of GQDs (a), g-C$_3$N$_4$, and 5CD@g-C$_3$N$_4$ (b).

introduction of mig-gap impurity levels within the band-gap of g-C$_3$N$_4$. The optical direct band gaps of the as-synthesized materials were determined based on the Kubelka-Munck theory as in Equation (2) [58].

$$(\alpha h\nu)^2 = k \ (h\nu - E_g) \tag{Eq. 2}$$

where E_g (eV), α, h (J.s), and v (s^{-1}) represent the band-gap energy, the absorption coefficient, the Planck constant and the optical frequency, respectively [59].

The band-gap energy of g-C$_3$N$_4$ determined by Eq. (1) decreased with the introduction of GQDs to the g-C$_3$N$_4$ lattice (Table 1). The narrow band-gap was due to the presence of mid-gap levels between the bulk g-C$_3$N$_4$ and GQDs, which was mainly derived from the delocalization of π electrons in the aromatic rings of CD@g-C$_3$N$_4$ [60]. This phenomenon is really useful for the utilization of light which promotes the generation of photo-induced charge carriers for photocatalytic activity [61].

3.3. Photocatalytic performance of CD@g-C$_3$N$_4$ photocatalysts

3.3.1. Effects of GQDs loadings

The photocatalytic performance of CD@g-C$_3$N$_4$ with different loadings of GQDs was evaluated through the degradation of TC (40 mg L^{-1}) at pH 4.2 (no pH adjustment) under UV light irradiation. As shown in Fig. 6, about 41% of the TC was degraded without any addition of photocatalysts, indicating that the photolysis of TC was significant under the irradiation condition. By adding the bulk g-C$_3$N$_4$ to the photocatalytic system, it is noted that 5% of TC was removed within 90 min under the dark condition due to the adsorption powered by the bulk g-C$_3$N$_4$, while 83% was removed within 120 min due to the photocatalysis driven by the bulk g-C$_3$N$_4$. Interestingly, these processes were more efficient in the presence of CD@g-C$_3$N$_4$ samples due to the higher surface areas, more active sites, narrower band-gaps, and better photo-generated electrons and holes in CD@g-C$_3$N$_4$, which will be discussed later, compared to the pristine g-C$_3$N$_4$. About 10% of the TC was adsorbed by these two samples within 90 min. The adsorption values were slightly higher than the value of the bulk g-C$_3$N$_4$ owing to the presence of functional groups of GQDs at low levels. Under light irradiation, the CD@g-C$_3$N$_4$ photocatalysts showed a 94–96% TC alleviation efficiency in 120 min, attributed to their specific textural structures leading to higher photocatalytic activity. Amongst the CD@g-C$_3$N$_4$ samples, 5CD@g-C$_3$N$_4$ showed the highest and comparative alleviation of TC, driven by both adsorption and photocatalysis. The results show that the amount of GQDs deposited on g-C$_3$N$_4$ affected the photocatalytic performance of the photocatalysts.

3.3.2. Effects of TC concentration

In order to study the effects of the concentration of the target contaminant on the TC alleviation, different concentrations of TC (10, 20, 30, and 40 mg L^{-1}) were applied to the photocatalytic system, while the initial pH values of the solutions were set at 4.2. As shown in Fig. 7, about 63% of the TC was degraded without adding any photocatalysts, as the concentration of TC was 10 mg L^{-1}. This value was recorded as 41 % at 40 mg L^{-1} of TC. The results show that the photolysis of TC is highly dependent on its concentration. The photolysis of TC was severe at its low concentration but alleviated at its high concentration, which is consistent with the previous report [62]. In the presence of 5CD@g-C$_3$N$_4$, it can be observed that 21% of TC (10 mg L^{-1}) was ameliorated through the adsorption on the photocatalyst in the dark condition. As the TC concentration increased to 20 mg L^{-1}, the TC adsorption efficiency of 5CD@g-C$_3$N$_4$ decreased to 10%, and was stable at the higher concentrations of 30 and 40 mg L^{-1}. This can be explained by the fact that 5CD@g-C$_3$N$_4$ was able to adsorb the TC molecules at TC concentrations lower than 10 mg L^{-1} with the aid of its available functional groups and porous structure, but its surface became occupied and saturated by the adsorbed molecules at higher concentrations of TC due to the limited availability of its functional groups and the comparative adsorption of the adsorbed molecules [63]. Under UV light exposure,
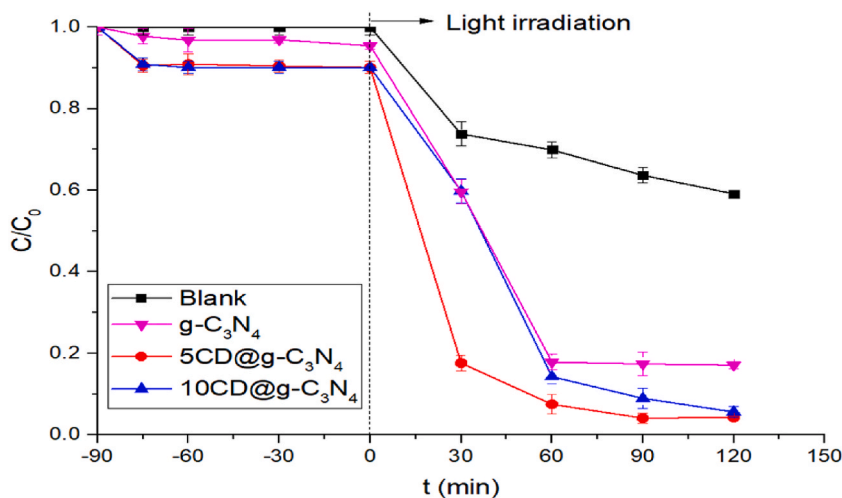

Fig. 6. The photocatalytic performance of g-C$_3$N$_4$ and CD@g-C$_3$N$_4$ with different loadings of GQDs.
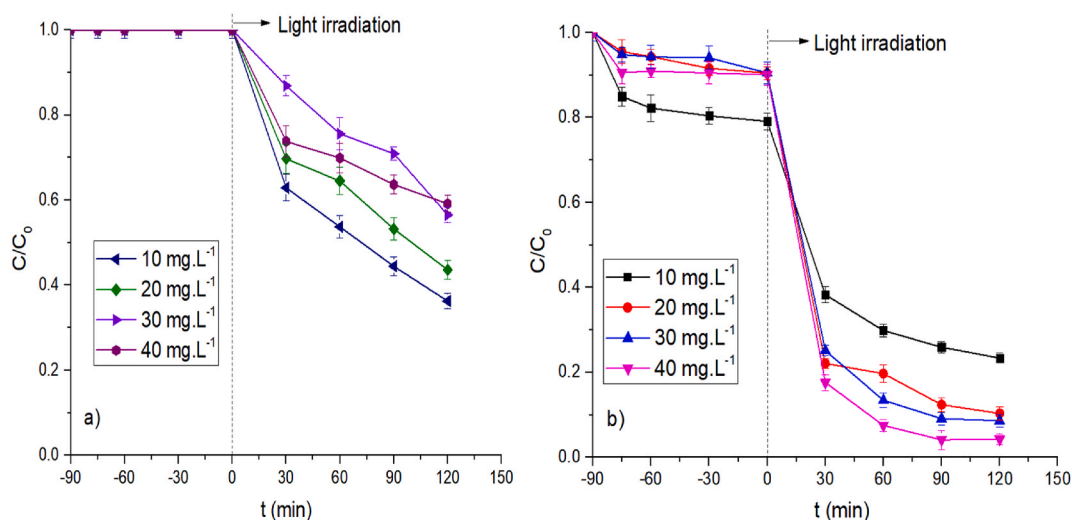
Fig. 7. Effects of the concentration of the target contaminant on TC alleviation without (a) and with (b) 5CD@g-C_3N_4 under light irradiation.

the opposite trend of photocatalysis was observed for 5CD@g-C_3N_4, which displayed 76%, 89%, 91% and 96% of photocatalytic efficiency for 10, 20, 30, and 40 mg L^{-1} of TC, respectively. This is due to the low accessibility of TC molecules to the active sites and photo-induced radicals at low concentrations of TC, which resulted in low photocatalytic efficiency. As compared to other g–C_3N_4–based photocatalysts, our CD@g-C_3N_4 photocatalysts showed the positive outcome of photo-degradation efficiency of TC (Table 2).

3.3.3. Effects of pH solution

The pH of the solution is another parameter that strongly affected the photolysis of TC and its adsorption (in the dark) as well as its photo-degradation (under the light irradiation) over the photocatalysts. The TC solution (40 mg L^{-1}) was adjusted to different pH values (2–10) to study the pH-dependent characteristics of these processes. It is well known that TC is an amphiphilic molecule (pK_{a1} = 3.3, pK_{a2} = 7.7, and pK_{a3} = 9.7) that exists in different species, such as TCH_3^+, TCH_2, TCH^-, and TC^{2-}, depending on the pH of the solution [67]. The UV–Vis spectra of TC (Fig. 8a) shows that the absorbance of TC increased with the increase in pH due to the increase in the electron density of the TC molecules, which changed the bond orbital energy of the molecules and led to different light absorption rates among the different TC species [68]. This also revealed that the negatively charged species of TC exhibited higher extinction efficiency than its neutral and positively charged species [68], evidenced by the higher rate constants of the photolysis of TC at higher pH values (see Section 3.3.4). Moreover, the characteristic peak of TC was seen to be red-shifted at the higher alkalinity of the TC solution due to the transformation of TC species related to the π- π * transition (HOMO-1 to LUMO) of TC chromophore. Additionally, a broad peak at 537 nm was observed in the UV–Vis spectrum of TC during photolysis at pH 10, which is an indicator of the formation of 4a, 12a-anhydro-4-oxo-4-dedimethylaminotetracycline (a photolysis product) [69]. The change in the color of the TC solution from yellow to pink during photolysis was also recorded at pH 8 and 10 (Fig. 8a, the inset), indicating the formation of polar intermediates derived from the loss of functional moiety in the TC molecules. It can be deduced from Fig. 8b that at pH 2, where TC is dominantly in the form of TCH_3^+ [63], 21% of TC was degraded without any photocatalyst. The increase in the alkalinity of the TC solution led to an increase in the photolysis of TC up to 75% at pH 10 where TCH^- and TC^{2-} are the dominant species [63,67]. The results indicate that the high alkalinity of the TC solution boosted its photolysis.

The adsorption and photocatalytic efficiencies of TC over g-C_3N_4 and 5CD@g-C_3N_4 are shown in Fig. 9. In terms of adsorption efficiency, 5CD@g-C_3N_4 showed an enhancement in TC adsorption within 90 min compared to the bulk of g-C_3N_4 over the entire investigated pH. An increase in pH solution resulted in a decrease in adsorption efficiency. Similarly, in terms of photocatalytic efficiency, 5CD@g-C_3N_4 exhibited superior photocatalytic activity compared to g-C_3N_4 regarding the photo-degradation of TC within 120 min. About 96% of the TC (40 mg L^{-1}) was removed by 5CD@g-C_3N_4 at pH 2 or 4, while 91% and 83% of TC's alleviation efficiency was recorded on g-C_3N_4 at pH 2 and pH 4, respectively. The efficiencies declined with the increased pH. However, the TC

Table 2

Comparison of photo-degradation efficiency of TC over g–C_3N_4–based photocatalysts.

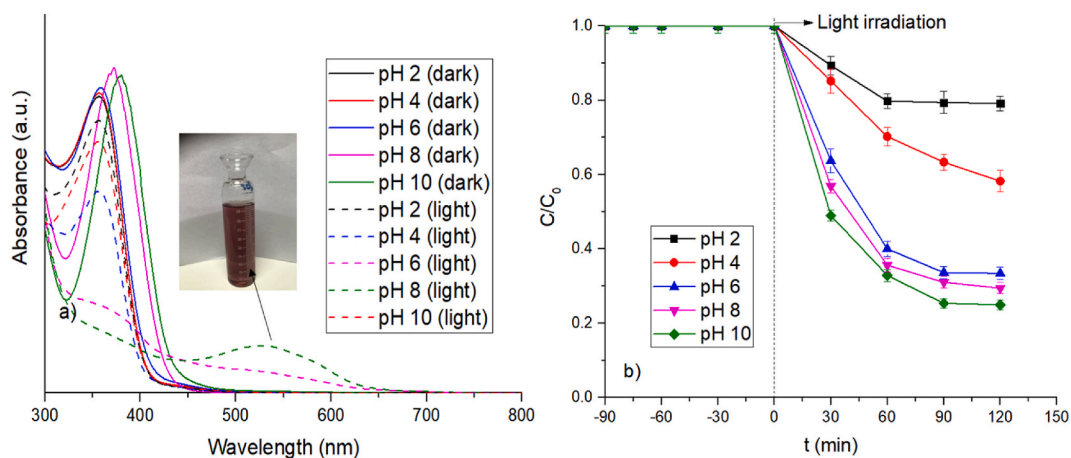| No.	Photocatalyst	Light source	Efficiency (%)/time (min)	Ref.
1.	GQDs loaded mpg-C_3N_4	Xe arc lamp	70/120	[49]
2.	Bi_2WO_6 nanosheets loaded g-C_3N_4 QDs	Xe arc lamp	87/60	[64]
3.	carbon dots decorated graphitic carbon/persulfate	LED	82/120	[65]
4.	N-GQD/g-C_3N_4	Xe arc lamp	72/180	[66]
5.	GQD@g-C_3N_4	LED	96/120	This study

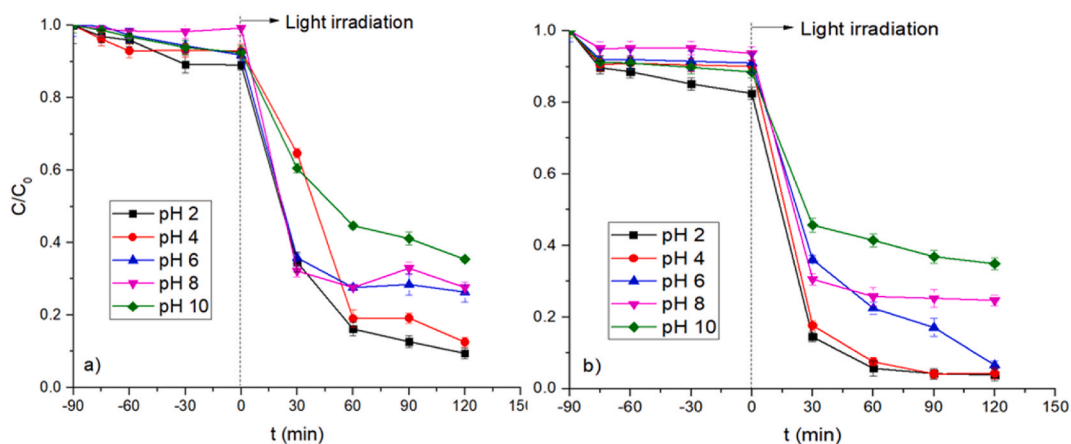**Fig. 8.** Effects of pH on the photolysis of TC in the dark and under UV light irradiation.

Fig. 9. Effects of pH on the photocatalytic performance of (a) g-C$_3$N$_4$ and (b) 5CD@g-C$_3$N$_4$ under UV light irradiation.

alleviation efficiencies at a certain pH value outweighed the photolysis efficiency under the same pH condition, suggesting that the TC alleviation in the presence of the photocatalysts was mainly driven by their photocatalytic activity.

3.3.4. Kinetics study

We also investigated the reaction kinetics of the photolysis of TC and its photocatalytic degradation by g-C$_3$N$_4$ and CD@g-C$_3$N$_4$
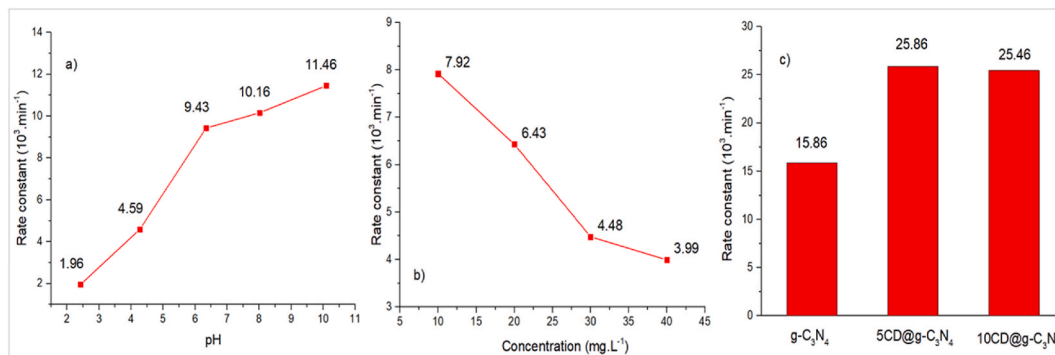

Fig. 10. The rate constants of the photolysis of TC at different pHs (a) and concentrations of TC (b). The rate constants of the photo-degradation of TC over g-C$_3$N$_4$ and CD@g-C$_3$N$_4$ photocatalysts (c).

samples using the following pseudo-first-order (Eq. (3)) kinetic models:

$$\ln \frac{C_0}{C} = at \qquad \text{(Eq. 3)}$$

where t is the irradiation time (min), C_0 and C (mg.L^{-1}) are the initial concentrations of TC and its concentration at time t, respectively, and a (min^{-1}) is the reaction rate constant. As shown in Fig. 10, the rate constant of the photolysis was elevated at high pH values in the TC solution but declined at its high concentrations, indicating that the photolysis of TC was favorable in its alkaline medium and at its low concentration. When it comes to photocatalytic degradation by g-C_3N_4 and CD@g-C_3N_4 photocatalysts, the CD@g-C_3N_4 samples exhibited higher rate constants than the rate constant of bulk g-C_3N_4 due to their higher porosity, narrower band gaps, better light absorption abilities, and effective separation of photo-induced charge carriers [70]. However, the photocatalysis over CD@g-C_3N_4 became slower at high loadings of GQDs.

3.4. Adsorption and photocatalysis mechanisms

The adsorption of TC by g-C_3N_4 and CD@g-C_3N_4 photocatalysts strongly depends on the structures, functional groups, and charges of the TC, g-C_3N_4, and CD@g-C_3N_4 photocatalysts. The charges varied depending on the pH value. The point of zero charge (PZC) of g-C_3N_4 was reported to be 2.52 [29]. Therefore, the material was negatively charged over the entire investigated pH range. Meanwhile, TC exhibited positive charges at pH < 3.3. Under this pH condition, the possible adsorption mechanisms included an electronic attraction between the positively charged TCH_3^+ and negatively charged g-C_3N_4, and a cation-π interaction between TCH_3^+ and the π system on g-C_3N_4, π-π interaction between the π systems of TC and g-C_3N_4, hydrogen bonding, and pore filling. At 3.3 < pH < 7.7, there were no net electrical charges for TC. Hence, it is rare for TC to introduce cation-π interaction and electronic attraction with g-C_3N_4, making the adsorption efficiency decrease with the increased pH. When the pH > 7.7, TC was in the form of TCH^- and TC^{3-}, which showed repulsion to g-C_3N_4. Compared to g-C_3N_4, the CD@g-C_3N_4 samples exhibited a higher adsorption ability than g-C_3N_4 due to the negatively charged surface of the graphene-based materials in the presence of carboxylic, hydroxyl, aldehyde, and ketone groups [71, 72].

To gain an understanding of the photocatalysis mechanism driven by radical species, a variety of radical scavengers were added to the reaction system. Generally, IPA (·OH quencher), KI (h^+ quencher), and BQ (·O_2^- quencher) are employed during the photocatalytic degradation of TC [73]. As shown in Fig. 11a and b, the TC alleviation decreased in the presence of these scavengers compared to without them. This implied that ·OH, h^+ and ·O_2^- were involved in the photocatalytic degradation of TC. The alleviation of TC was highly suppressed by BQ, indicating that ·O_2^- was the key radical species during the photocatalytic degradation.

The potentials of the conduction band (CB) and valence band (VB) of g-C_3N_4 were estimated using Equations (4) and (5):

$$E_{VB} = \chi - E_e + 0.5E_g \qquad \text{(Eq. 4)}$$

$$E_{CB} = E_{VB} - E_g \qquad \text{(Eq. 5)}$$

where χ and E_e represent the electronegativity of the semiconductor and energy of the free electrons, respectively. E_g is the band gap energy of the semiconductor. χ is 4.72 eV, E_e is 4.5 eV (vs. NHE), and E_g is 2.81 eV. Therefore, E_{VB} and E_{CB} of g-C_3N_4 were estimated at 1.62 eV and −1.19 eV, respectively. With its band gap energy, g-C_3N_4 enabled its photo-excited electrons (e^-) to migrate from its VB into CB and to leave photo-excited holes (h^+) in its VB under UV light irradiation (Eq. (6)). Due to the more negative E_{CB} of g-C_3N_4 than the reduction potential of O_2/·O_2^- (−0.33 eV vs. NHE), the electrons (e^-) reduce the dissolved O_2 molecules in the TC solution to form superoxide (·O_2^-) radicals (Eq. (8)), further oxidizing TC to degraded products (Eq. (10)). Moreover, TC can be oxidized directly by the holes (h^+) in the VB (Eq. (10)), or by hydroxyl (·OH) radicals generated by the reaction between ·O_2- and water (Eq. (9)) [74]. However, h^+ could not oxidize the H_2O molecules and hydroxide (OH^-) to form hydroxyl (·OH) radicals because the VB of g-C_3N_4 was less positive than the reduction potential of H_2O/·OH (+2.38 eV vs. NHE) and OH^-/·OH (+1.99 eV vs. NHE). With the aid of GQDs as a photosensitizer, more photo-excited electrons were inserted into the CB of g-C_3N_4 by their migration from the CB of GQDs (Eq. (7)) to that of g-C_3N_4 under UV light irradiation. Moreover, the GQDs also acted as a place to trap electrons injected from its CB into that of g-C_3N_4, thus enhancing the photocatalytic activity of CD@g-C_3N_4. As a result of that, 5CD@g-C_3N_4 showed higher intensity of its photocurrent than that of g-C_3N_4 under the light irradiation, indicating its better ability of generation and separation of e^- and h^+ (Fig. 11c). The formation of the photo-induced charges and degradation reactions are proposed in Equations (6)–(10):

$$\text{g-}C_3N_4 + h\nu \rightarrow e^- \text{ (CB)} + h^+ \text{ (VB)} \qquad \text{(Eq. 6)}$$

$$\text{GQDs} + h\nu \rightarrow e^- \text{ (CB)} + h^+ \text{ (VB)} \qquad \text{(Eq. 7)}$$

$$O_2 + e^- \rightarrow ·O_2^- \qquad \text{(Eq. 8)}$$

$$·O_2^- + H_2O \rightarrow ·OH + OH^- \qquad \text{(Eq. 9)}$$

$$·O_2^-/·OH/ \, h^+ + TC \rightarrow \text{degradation products } (CO_2, H_2O \ldots) \qquad \text{(Eq. 10)}$$
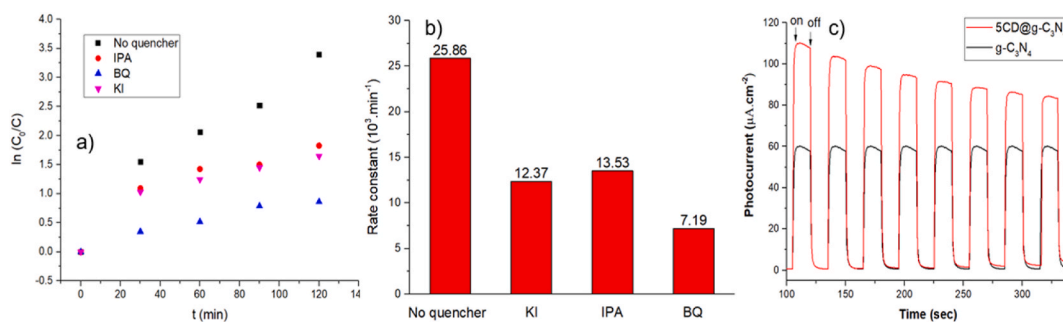
Fig. 11. (a,b) The rate constants of the photo-degradation of TC over 5CD@g-C$_3$N$_4$ in the presence of different quenchers. (c) Transient photo-current response of g-C$_3$N$_4$ and 5CD@g-C$_3$N$_4$ under UV light irradiation.

3.5. Application to treat the wastewater from a shrimp farm pond

For the application of photocatalysts to local-shrimp-pond-derived wastewater, the wastewater was taken from an in-situ-RAS-like shrimp pond located at the Institute for Environment and Resources at the National University of Ho Chi Minh City. The image of the pond is shown in Fig. 12. The water used for the pond was passed through a settlement tank and a series of vegetable containers before its return to the pond.

50.0 mL of the wastewater containing TC was taken from a RAS shrimp pond and stored in a 250 mL glass beaker in the presence of 0.08 g of 5CD@g-C$_3$N$_4$ photocatalyst under UV light irradiation for an hour. As seen in Fig. 13, about 5 % of the COD (chemical oxygen demand) was decreased and more than 90% of the TC was washed out of the wastewater after the treatment. Meanwhile, 27% of the TOC (total organic carbon) in the wastewater was reduced by the photocatalyst, indicating its ability to completely degrade organic compounds into CO$_2$ and H$_2$O. The results indicate that the CD@g-C$_3$N$_4$ photocatalysts are able to effectively degrade TC and other organic compounds in the shrimp pond.

Using the above results, we propose a modified RAS system for the future treatment of antibiotics and other organic pollutants. The system was modified by the addition of photocatalytic tanks, as described in Fig. 14. The wastewater from the shrimp pond (1) was passed through three consecutive tanks including two settlement tanks and a photocatalytic treatment tank between them, followed by a series of vegetable containers (2) before its return to the pond (3).

4. Conclusion

In this study, thermal polymerization and a hydrothermal treatment were utilized to successfully synthesize CD@g-C$_3$N$_4$ photo-catalysts. The characterization results unveiled the successful introduction of GQDs into the exfoliated g-C$_3$N$_4$ matrix which enhanced its surface area and light absorption ability, resulting in the improved photocatalytic activity involved in the photo-degradation of TC. The photocatalytic efficiencies declined with an increase in the pH of the solution which in turn boosted the photolysis of TC. Moreover, the amount of GQDs deposited on g-C$_3$N$_4$ strongly affected the photocatalytic performance of the photocatalysts. Low loadings of GQDs over g-C$_3$N$_4$ resulted in a faster and more effective photocatalysis of TC. $\cdot$OH, h$^+$ and $\cdot$O$_2^-$ were involved in the photocatalytic degradation of TC in which $\cdot$O$_2^-$ was the key radical species. Practically, CD@g-C$_3$N$_4$ photocatalysts are applicable in the degradation of organic compounds discharged from the wastewater of a RAS shrimp pond into CO$_2$ and H$_2$O.
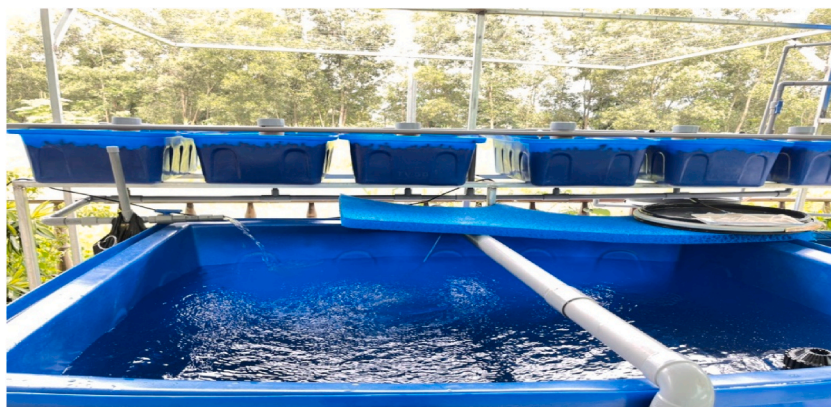

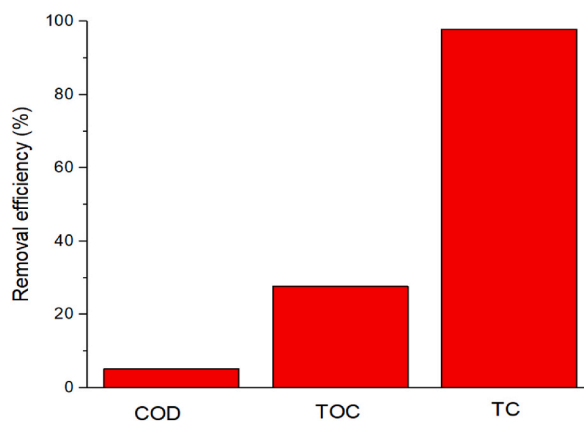**Fig. 12.** Current set-up of the in-situ RAS shrimp farming pond.

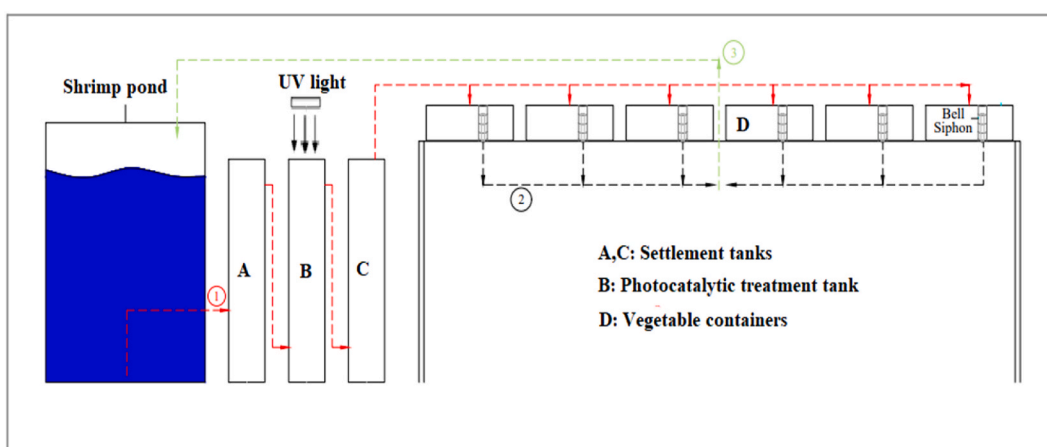**Fig. 13.** Wastewater quality after the treatment with 5CD@g-C$_3$N$_4$.

Fig. 14. Schematic set-up of a proposed RAS shrimp farming pond.

Data statements

All of the data were included in the manuscript.

CRediT authorship contribution statement

Nguyen Thi Phuong Thao: Writing – original draft, Methodology, Investigation, Data curation. **Nguyen Le Minh Tri:** Writing – review & editing, Writing – original draft, Methodology, Investigation, Formal analysis, Data curation, Conceptualization. **Tran Trung Kien:** Writing – original draft, Validation, Resources, Investigation, Formal analysis, Data curation. **Tra Van Tung:** Writing – review & editing, Project administration, Funding acquisition, Conceptualization. **Tran Thi Hieu:** Writing – original draft, Visualization, Investigation, Data curation. **Nguyen Viet Thang:** Investigation, Formal analysis, Data curation. **Le Thanh Son:** Writing – review & editing, Writing – original draft, Validation, Resources, Methodology. **Tran Le Luu:** Writing – review & editing, Writing – original draft, Supervision, Formal analysis, Conceptualization. **Hans Schnitzer:** Writing – review & editing, Supervision, Methodology, Conceptualization. **Hai Le Thanh:** Writing – review & editing, Supervision, Project administration, Funding acquisition, Conceptualization.

Declaration of competing interest

The authors declare that they have no known competing financial interests or personal relationships that could have appeared to influence the work reported in this paper.

Acknowledgments

This research is funded by Vietnam National University - Ho Chi Minh City (VNU-HCM) under grant number DN-2022-24-01. The authors would like to thank to the local authorities and households in the Mekong delta for assistance during site investigation and data collection, and the research group at IPPE, TU Graz, Austria, for the collaboration to implement this study.

References

[1] J. Chen, et al., Structural design of carbon dots/porous materials composites and their applications, Chem. Eng. J. (2020) 127743.
[2] J. Liu, et al., Metal-free efficient photocatalyst for stable visible water splitting via a two-electron pathway, Science 347 (6225) (2015) 970.
[3] D. Ghosh, et al., Current and future perspectives of carbon and graphene quantum dots: from synthesis to strategy for building optoelectronic and energy devices, Renew. Sustain. Energy Rev. 135 (2021) 110391.
[4] S. Tachi, et al., Quantum Yield enhancement in graphene quantum dots via esterification with benzyl alcohol, Sci. Rep. 9 (1) (2019) 14115.
[5] K. Murugan, et al., Nanofabrication of graphene quantum dots with high toxicity against malaria mosquitoes, plasmodium falciparum and MCF-7 cancer cells: impact on predation of non-target tadpoles, odonate nymphs and mosquito fishes, J. Cluster Sci. 28 (1) (2017) 393–411.
[6] G. Xie, et al., Graphene-based materials for hydrogen generation from light-driven water splitting, Adv. Mater. 25 (28) (2013) 3820–3839.
[7] M. Morsy, et al., Design and implementation of humidity sensor based on carbon nitride modified with graphene quantum dots, Sci. Rep. 13 (1) (2023) 2891.
[8] K. Akimoto, et al., Assessment of the emission reduction target of halving CO_2 emissions by 2050: macro-factors analysis and model analysis under newly developed socio-economic scenarios, Energy Strategy Rev. 2 (3) (2014) 246–256.
[9] C.W. Kim, et al., Artificial photosynthesis for formaldehyde production with 85% of faradaic efficiency by tuning the reduction potential, ACS Catal. 8 (2) (2018) 968–974.
[10] J. Albo, et al., Use of an optofluidic microreactor and Cu nanoparticles synthesized in ionic liquid and embedded in TiO_2 for an efficient photoreduction of CO_2 to methanol, Chem. Eng. J. 404 (2021) 126643.
[11] T.P. Yendrapati Taraka, et al., Controlled addition of Cu/Zn in hierarchical CuO/ZnO p-n heterojunction photocatalyst for high photoreduction of CO_2 to MeOH, J. CO_2 Util. 31 (2019) 207–214.
[12] Z. Huang, et al., A ZIF-8 decorated TiO_2 grid-like film with high CO_2 adsorption for CO_2 photoreduction, J. CO_2 Util. 24 (2018) 369–375.
[13] Z. Duan, et al., Ag-Bi/BiVO4 chain-like hollow microstructures with enhanced photocatalytic activity for CO_2 conversion, Appl. Catal. Gen. 594 (2020) 117459.
[14] S. Wang, et al., Effective separation and transfer of carriers into the redox sites on Ta3N5/Bi photocatalyst for promoting conversion of CO_2 into CH4, Appl. Catal. B Environ. 224 (2018) 10–16.
[15] M.J. Kang, et al., Selective alcohol on dark cathodes by photoelectrochemical CO_2 valorization and their in situ characterization, ACS Energy Lett. 4 (7) (2019) 1549–1555.
[16] D.-T. Nguyen, C.-C. Nguyen, T.-O. Do, Rational one-step synthesis of cobalt clusters embedded-graphitic carbon nitrides for the efficient photocatalytic CO_2 reduction under ambient conditions, J. Catal. 392 (2020) 88–96.
[17] S. Zhang, et al., Enhanced photocatalytic removal of antibiotics over graphitic carbon nitride induced by acetic acid post-treatment, Colloids Surf. A Physicochem. Eng. Asp. 664 (2023) 131165.
[18] T. Muhmood, A. Uddin, Fabrication of spherical-graphitic carbon nitride via hydrothermal method for enhanced photo-degradation ability towards antibiotic, Chem. Phys. Lett. 753 (2020) 137604.
[19] D. Van Thuan, et al., Development of Indium vanadate and Silver deposited on graphitic carbon nitride ternary heterojunction for advanced photocatalytic degradation of residual antibiotics in aqueous environment, Opt. Mater. 123 (2022) 111885.
[20] J. Zhong, et al., Simultaneous removal of micropollutants, antibiotic resistant bacteria, and antibiotic resistance genes using graphitic carbon nitride under simulated solar irradiation, Chem. Eng. J. 433 (2022) 133839.
[21] T.H. Pham, et al., Graphitic carbon nitride metal-free photocatalyst for the simultaneous removal of emerging pharmaceutical pollutants in wastewater, Environ. Res. 231 (2023) 116246.
[22] X. Wang, et al., Synthesis of K-doped g-C3N4/carbon microsphere@graphene composite with high surface area for enhanced adsorption and visible photocatalytic degradation of tetracycline, J. Taiwan Inst. Chem. Eng. 91 (2018) 609–622.
[23] A. Wang, et al., Recent advances of graphitic carbon nitride-based structures and applications in catalyst, sensing, imaging, and LEDs, Nano-Micro Lett. 9 (4) (2017) 47.
[24] J. Wang, et al., 3D/2D direct Z-scheme heterojunctions of hierarchical TiO_2 microflowers/g-C3N4 nanosheets with enhanced charge carrier separation for photocatalytic H2 evolution, Carbon 149 (2019) 618–626.
[25] R. He, et al., Room-temperature in situ fabrication of Bi2O3/g-C3N4 direct Z-scheme photocatalyst with enhanced photocatalytic activity, Appl. Surf. Sci. 430 (2018) 273–282.
[26] M. Jourshabani, et al., Superior photodegradation of organic compounds and H2O2 production over tungsten oxide/carbon nitride heterojunction with sizable heptazine units: dual polycondensation and interface engineering, Chem. Eng. J. 427 (2022) 131710.
[27] L. Jiang, et al., Nitrogen self-doped g-C3N4 nanosheets with tunable band structures for enhanced photocatalytic tetracycline degradation, J. Colloid Interface Sci. 536 (2019) 17–29.
[28] H. Yuan, et al., Dual-channels separated mechanism of photo-generated charges over semiconductor photocatalyst for hydrogen evolution: interfacial charge transfer and transport dynamics insight, Chem. Eng. J. 454 (2023) 140442.
[29] T.S. Bui, et al., Facile fabrication of novel Ba-doped g-C3N4 photocatalyst with remarkably enhanced photocatalytic activity towards tetracycline elimination under visible-light irradiation, Appl. Surf. Sci. 506 (2020) 144184.
[30] X. Yang, et al., In situ synthesis of 2D ultrathin cobalt doped g-C3N4 nanosheets enhances photocatalytic performance by accelerating charge transfer, J. Alloys Compd. 859 (2021) 157754.
[31] Y. Fao, Fishery and Aquaculture Statistics, Food and Agriculture Organization of the United Nations, 2016, p. 11.
[32] A.R. Dhar, M.T. Uddin, M.K. Roy, Assessment of organic shrimp farming sustainability from economic and environmental viewpoints in Bangladesh, Environ. Res. 180 (2020) 108879.
[33] K. Thornber, et al., Evaluating antimicrobial resistance in the global shrimp industry, Rev. Aquacult. 12 (2) (2020) 966–986.
[34] L. Camacho-Jiménez, A.R. Álvarez-Sánchez, C.H. Mejía-Ruíz, Silver nanoparticles (AgNPs) as antimicrobials in marine shrimp farming: a review, Aquaculture Reports 18 (2020) 100512.
[35] H. Fourooghifard, et al., Nitrogen and phosphorous budgets for integrated culture of Litopenaeus vannamei with red sea algae Gracilaria corticata under zero water exchange system, Iran. J. Fish. Sci. 17 (3) (2018) 471–486.
[36] S.J. Funge-Smith, M.R.P. Briggs, Nutrient budgets in intensive shrimp ponds: implications for sustainability, Aquaculture 164 (1) (1998) 117–133.
[37] T.T. Kien, et al., Nitrogen conversion efficiency in the integrated catfish farming system toward closed ecosystem in Mekong delta, Vietnam, Process Saf. Environ. Protect. 168 (2022) 180–188.
[38] S. O, G. Santos, Pharmaceutical contaminants: ecotoxicological aspects and recent advances in oxidation technologies for their removal in aqueous matrices, J. Environ. Chem. Eng. 10 (6) (2022) 108932.
[39] X.-D. Zhu, et al., Photocatalytic degradation of tetracycline in aqueous solution by nanosized TiO_2, Chemosphere 92 (8) (2013) 925–932.
[40] J. Chen, et al., Enhanced solar-induced photocatalytic removal of antibiotics over molecularly reconstituted graphitic carbon nitride, Appl. Surf. Sci. 634 (2023) 157637.

[41] M. Cui, et al., Synergistic effect of mesoporous graphitic carbon nitride and peroxydisulfate in visible light-induced degradation of atenolol: a combined experimental and theoretical study, Chem. Eng. J. 412 (2021) 127979.

[42] W. Dong, et al., Optimized removal of antibiotics over Cd0.5Zn0.5S/NiCo-LDH : Constructing a homojunctions-heterojunctions composite photocatalyst, J. Environ. Chem. Eng. 10 (6) (2022) 108624.

[43] R.N. Juine, B.K. Sahu, A. Das, ZnS nano-photocatalysts with elemental type s defects for the visible light harvest and efficient antibiotic, explosive and azo dye pollutants degradation, J. Environ. Chem. Eng. 11 (6) (2023) 111175.

[44] F. Conzuelo, et al., Disposable amperometric magneto-immunosensor for direct detection of tetracyclines antibiotics residues in milk, Anal. Chim. Acta 737 (2012) 29–36.

[45] Q.H. Luu, et al., Antibiotics use in fish and shrimp farms in Vietnam, Aquaculture Reports 20 (2021) 100711.

[46] Y. Xiao, et al., Molecule self-assembly synthesis of porous few-layer carbon nitride for highly efficient photoredox catalysis, J. Am. Chem. Soc. 141 (6) (2019) 2508–2515.

[47] K. Zhang, et al., Iron phthalocyanine nanodots decorated ultra-thin porous carbon nitride: a combination of photocatalysis and Fenton reaction to achieve two-channel efficient tetracycline degradation, J. Alloys Compd. 966 (2023) 171580.

[48] P. Niu, et al., Graphene-like carbon nitride nanosheets for improved photocatalytic activities, Adv. Funct. Mater. 22 (22) (2012) 4763–4770.

[49] J. Liu, et al., Graphene quantum dots modified mesoporous graphite carbon nitride with significant enhancement of photocatalytic activity, Appl. Catal. B Environ. 207 (2017) 429–437.

[50] Y. Liu, C.-y. Liu, Z.-y. Zhang, Synthesis of highly luminescent graphitized carbon dots and the application in the Hg2+ detection, Appl. Surf. Sci. 263 (2012) 481–485.

[51] Y. Deng, et al., Construction of plasmonic Ag and nitrogen-doped graphene quantum dots codecorated ultrathin graphitic carbon nitride nanosheet composites with enhanced photocatalytic activity: full-spectrum response ability and mechanism insight, ACS Appl. Mater. Interfaces 9 (49) (2017) 42816–42828.

[52] M.-T. Nguyen-Le, B.-K. Lee, Effective photodegradation of dyes using in-situ N-Ti3+ co-doped porous titanate-TiO2 rod-like heterojunctions, Catal. Today 297 (2017) 228–236.

[53] M. Razavi-Esfali, et al., Highly efficient photocatalytic degradation of organic pollutants by mesoporous graphitic carbon nitride bonded with cyano groups, Chem. Eng. J. 419 (2021) 129503.

[54] M.-T. Nguyen-Le, B.-K. Lee, D.-M. Tran, EDTA-Na2-assisted synthesis of rod-like titanate-TiO2 composite architectures with enhanced visible-light-driven properties, J. Ind. Eng. Chem. 56 (2017) 225–234.

[55] Y. Jiao, et al., A novel MoS2 quantum dots (QDs) decorated Z-scheme g-C3N4 nanosheet/N-doped carbon dots heterostructure photocatalyst for photocatalytic hydrogen evolution, Appl. Catal. B Environ. 247 (2019) 124–132.

[56] S. Asadzadeh-Khaneghah, A. Habibi-Yangjeh, M. Abedi, Decoration of carbon dots and AgCl over g-C3N4 nanosheets: novel photocatalysts with substantially improved activity under visible light, Sep. Purif. Technol. 199 (2018) 64–77.

[57] W. Huang, et al., Photoluminescence of graphene quantum dots enhanced by microwave post-treatment, Chem. Eng. J. 405 (2021) 126714.

[58] W. Han, et al., Photocatalytic activation of peroxymonosulfate by surface-tailored carbon quantum dots, J. Hazard Mater. 395 (2020) 122695.

[59] Y. Deng, et al., Insight into highly efficient simultaneous photocatalytic removal of Cr(VI) and 2,4-dichlorophenol under visible light irradiation by phosphorus doped porous ultrathin g-C3N4 nanosheets from aqueous media: performance and reaction mechanism, Appl. Catal. B Environ. 203 (2017) 343–354.

[60] Y. Zhou, et al., N-doped graphitic carbon-incorporated g-C3N4 for remarkably enhanced photocatalytic H2 evolution under visible light, Carbon 99 (2016) 111–117.

[61] F. Wang, et al., Novel ternary photocatalyst of single atom-dispersed silver and carbon quantum dots co-loaded with ultrathin g-C3N4 for broad spectrum photocatalytic degradation of naproxen, Appl. Catal. B Environ. 221 (2018) 510–520.

[62] S. Jiao, et al., Aqueous photolysis of tetracycline and toxicity of photolytic products to luminescent bacteria, Chemosphere 73 (3) (2008) 377–382.

[63] C. Chen, X. Feng, S. Yao, Ionic liquid-multi walled carbon nanotubes composite tablet for continuous adsorption of tetracyclines and heavy metals, J. Clean. Prod. 286 (2021) 124937.

[64] M. Zhang, et al., Ultrathin Bi2WO6 nanosheets loaded g-C3N4 quantum dots: a direct Z-scheme photocatalyst with enhanced photocatalytic activity towards degradation of organic pollutants under wide spectrum light irradiation, J. Colloid Interface Sci. 539 (2019) 654–664.

[65] C. Yin, et al., Synergistic degradation of tetracycline by CDs decorated g-C3N4 under LED light irradiation combined with the persulfate-based advanced oxidation process, Appl. Catal. Gen. 636 (2022) 118571.

[66] H. Han, et al., Non-metallic nitrogen-doped graphene quantum dots coupled with g-C3N4 achieve efficient photocatalytic performance, Appl. Surf. Sci. 649 (2024) 159171.

[67] P. Wang, et al., Strong adsorption of tetracycline on octahedral Cu2O nanocrystals exposed with {111} facets: adsorption behavior and mechanism insight, Appl. Surf. Sci. 542 (2021) 148545.

[68] C. Song, et al., Photolysis mechanisms of tetracycline under UV irradiation in simulated aquatic environment surrounding limestone, Chemosphere 244 (2020) 125582.

[69] M. Addamo, et al., Removal of drugs in aqueous systems by photoassisted degradation, J. Appl. Electrochem. 35 (7) (2005) 765–774.

[70] A. Asadi, et al., Construction of Mg-doped ZnO/g-C3N4@ZIF-8 multi-component catalyst with superior catalytic performance for the degradation of illicit drug under visible light, Colloids Surf. A Physicochem. Eng. Asp. 650 (2022) 129536.

[71] R.H. Krishna, et al., Carbon nanotubes and graphene-based materials for adsorptive removal of metal ions – a review on surface functionalization and related adsorption mechanism, Applied Surface Science Advances 16 (2023) 100431.

[72] E. Boateng, et al., Functionalization of graphene-based nanomaterials for energy and hydrogen storage, Electrochim. Acta 452 (2023) 142340.

[73] X. Liu, et al., Insights into the evaluation of photocatalytic quenching experimental results by degrading a dye, Res. Chem. Intermed. 48 (7) (2022) 2915–2932.

[74] M. Morsy, et al., Highly efficient photocatalysts for methylene blue degradation based on a platform of deposited GO-ZnO nanoparticles on polyurethane foam, Molecules 28 (2023), https://doi.org/10.3390/molecules28010108.